THE JOURNAL OF PHYSICAL CHEMISTRY A
A JOURNAL OF THE AMERICAN CHEMICAL SOCIETY

Unveiling Optical Degradation under Irradiation-Driven Structural Damage of α-$CsPbI_3$ and α-$CsPbBrI_2$ via Combined DFT and Monte Carlo

Yibo Wang, Feida Chen,* Kun Yang, Daniu Han, and Xiaobin Tang*

Cite This: J. Phys. Chem. A 2025, 129, 4959−4967

ABSTRACT: All-inorganic lead-halide perovskites have emerged as promising photoelectronic materials for space applications due to their excellent optical properties and irradiation tolerance. However, a comprehensive understanding of the structure−function relationship between defects and properties is essential for their application. The present study employs density functional theory (DFT) data and Monte Carlo (MC) simulation to explore the effects of irradiation dissociation and displacement in $CsPbI_3$ and $CsPbBrI_2$ systems. The results demonstrate that $CsPbI_3$ and $CsPbBrI_2$ are more susceptible to damage at 50 keV, with $CsPbBrI_2$ exhibiting slightly higher damage under flux at 10^5 p/cm^2. The ab initio molecular dynamics (AIMD) and optical properties calculations indicate that $CsPbBrI_2$ possesses higher defect tolerance and optical stability, especially concerning lattice distortion induced by Frenkel defects. Our study provides a methodology for elucidating the impact of irradiation on the complex elementary perovskites and establishes a novel theoretical foundation for optical property changes with dynamic structure evolution under a radiation environment.

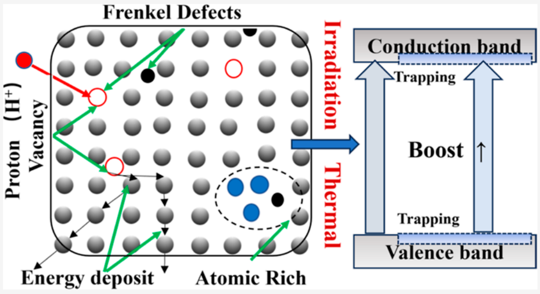

■ INTRODUCTION

The lead-halide perovskites (LHPs) are among the most promising optoelectronic materials with superior photovoltaic properties, which received considerable research due to their excellent light absorption, high mobility, and tunable band gap;[1,2] mainly, their photodetector properties can be used as optical sensors.[3−5] Organic and inorganic hybrid perovskites (OIHPs) were synthesized earlier compared to all inorganic perovskites (AIPs) with excellent power conversion efficiency (PCE) and are regarded as a potential alternative material to Si-based materials for future commercial photovoltaic materials in space. Studies have shown that current density (J_{sc}) and PCE were observed with a reduction of around 10% and 40% for proton doses of 10^{12} and 10^{16} p/cm^2, respectively, better than Si-based cells in a similar situation.[6] In particular, α-$CsPbI_3$ has excellent optical absorption and carrier mobility for photovoltaic devices.[7,8] Although it was previously reported that the $CsPbI_3$ phase was influenced by temperature,[9] the existing research has indicated the stability of the α-phase depends on the crystal size.[10,11] AIPs exhibited higher spatial stability due to the nonorganic composition of their A^+ position, which can decrease the spillage of organic components due to intensive ultraviolet.[12,13] The advantages utilization means the application prospect are that is more suitable for space environments with radiation environment, thermal cycling, and high vacuum conditions,[6,14] which arouse extensive discussion.

In the space environment, two main damage events, displacement damage and ionization damage, occurred during the designated service period.[15] The predominant source of ionization damage is an accumulation of charge photonics like X/γ-rays, which weaken the chemical bonds until they decompose. Displacement damage, on the other hand, is when the high-energy particles directly knock the atoms, resulting in the formation of Frenkel defects. Collision events are inevitable occurrences in the irradiation environments and exhibit a certain degree of continuity, leading to progressive lattice mismatch. This effect, along with increased dark current and parasitic field during carrier transport, causes the degradation of optical properties on the surface (such as reduced absorption, increased reflectivity, increased refraction, etc.). However, a comprehensive understanding of the irradiation−structure, damage−optical property relationship between irradiation and perovskites has not been fully achieved. In particular, the materials that consist of multiple elements with minimal discrepancies, for example, CsPb/Sn/Ag/Mn−Cl/Br/I et al., become exceedingly challenging for conventional molecular dynamics (MD) and Monte Carlo

Received: March 8, 2025
Revised: May 6, 2025
Accepted: May 13, 2025
Published: May 21, 2025

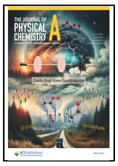

https://doi.org/10.1021/acs.jpca.5c01588

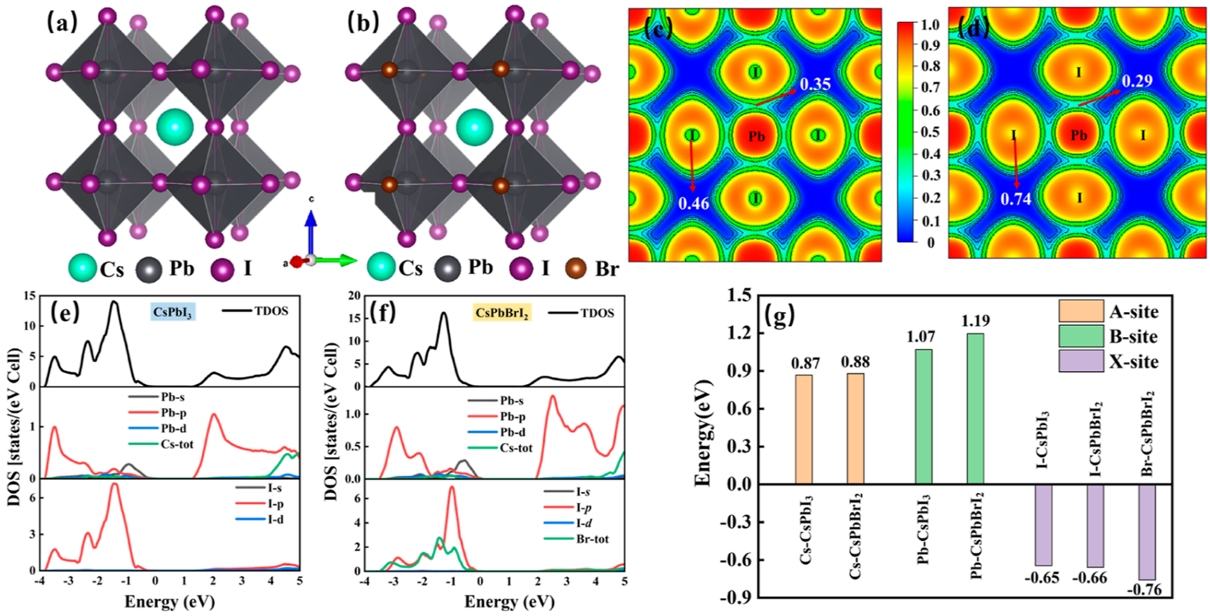

Figure 1. Schematic crystal structures of $CsPbI_3$ (a) and $CsPbBrI_2$ (b). The ELF of $CsPbI_3$ (c) and $CsPbBrI_2$ (d). Density of states (DOS) of $CsPbI_3$ (e) and $CsPbBrI_2$ (f). (g) The Bader charge transfer of $CsPbI_3$ and $CsPbBrI_2$.

(MC) methods to assess their irradiation capacity. The reasons can be attributed to three categories. (1) MD is used to employ large systems in irradiation simulations to accurately describe the primary knock-on atoms (PKA) process,[16,17] which depends on a high-quality potential field. The complexity of fitting the potential field due to the multi-elemental composition of perovskite makes it challenging to achieve. (2) Experimental observations of irreversible damage necessitate complex setups to collect data on performance, increasing costs.[15,17] (3) The coupling of ionization and displacement effects in the experiment obscures where the damage originates. Prior to conducting actual irradiation experiments, preliminary assessments of both penetration depth and radiation dosage are typically performed, with SRIM emerging as a predominant computational tool for such evaluations.[18−20] Nevertheless, the accuracy of MC simulations is limited by estimated parameters, particularly for multi-component systems, due to insufficient data on (1) the interatomic bond energy during collision events, (2) the minimum displacement threshold energy required for lattice site vacancy formation, and (3) the precise device layer thickness.

Previous research has investigated the phase degradation of LHPs after irradiation. The researchers found that the energy of irradiation dissociation of AIPs was higher after replacing MA^+ with Cs^+, implying that AIPs were more advantageous in terms of phase stability relative to OIHPs.[21] Xiao et al. compared the irradiation resistance of $MAPbI_3$ and $CsPbI_3$ using electron beams, demonstrating $CsPbI_3$'s enhanced stability.[22] The main displacement damage under 1 MeV electron beam irradiation is from H, C, N, and I atoms in OIHPs.[23] The defect of the I atoms through irradiation can act as an unintentional doping source and partially compensate deep traps, thereby avoiding the substantial degradation of carrier transport.[24] Moreover, a potential thermodynamic caused the phase transformation from the cubic phase (α-phase) to the orthorhombic phase (γ/δ-phase) in perovskites, which is detrimental to optical properties.[25] The reason is that the crystal structure, ambient temperature, and elemental composition can influence the dielectric functions, which are essential data for optical calculations. Various compositional engineering strategies, including A-site, B-site, and X-site doping, have been reported to enhance the stability of $CsPbI_3$.[26−30] Br doping in the Cs−Pb−I lattice to form $CsPbBrI_2$ improves both thermal and phase properties while maintaining favorable optical properties.[2] However, the atomic-scale mechanisms between irradiation dissociation and displacement damage in iodine-containing perovskites are incompletely understood.

Density functional theory (DFT) has been instrumental in computational investigations of irradiation-induced defects. Meanwhile, recent advances in ab initio molecular dynamics (AIMD) have provided researchers with a robust methodology for precisely determining displacement threshold energies. Herein, we propose a novel approach utilizing the DFT data passed to the MC as a pivotal input parameter for executing destructive irradiation simulations, ensuring a more accurate evaluation of irradiation damage in perovskite materials. The lattice binding energy, surface binding energy, and displacement threshold energy were calculated by DFT. SRIM code based on MC was employed to assess the displacement damage of $CsPbI_3$ and $CsPbBrI_2$. Furthermore, a mechanism explanation including lattice distortion and optical stability induced by Frenkel defects was discussed through the *NVT* ensemble. The present study provides potential insight into how radiation-induced defects affect the optical properties of $CsPbI_3$ and $CsPbBrI_2$. These findings substantially advance the development of perovskites as a radiation detector for application in space.

■ EXPERIMENTAL SECTION

DFT Calculation Details. The first principle calculations were implemented via Vienna ab initio simulation package (VASP) codes[31,32] and performed based on projector augmented wave (PAW) pseudopotential in reciprocal space by the generalized gradient approximation (GGA) with

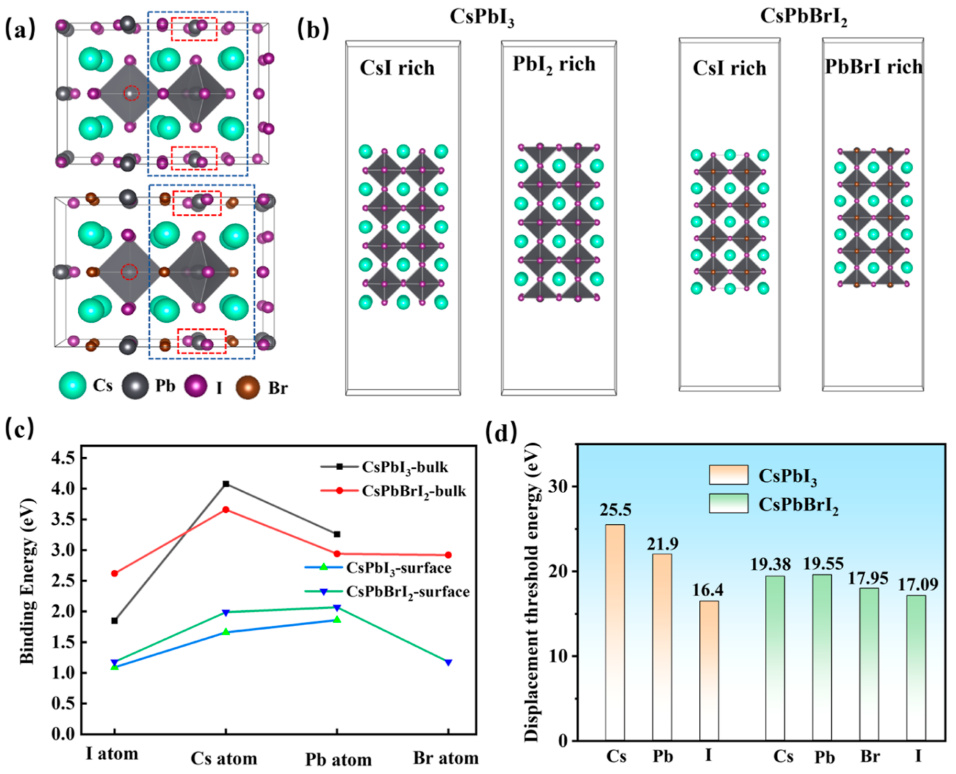

Figure 2. (a) The bulk structure of CsPbI$_3$ and CsPbBrI$_2$ used for the binding energy calculation. The red circles in the figure illustrate the vacancy of I. The blue dashed line shows the adjacent cell where the vacancy existed. The red dotted line shows the major mismatched Pb–I framework. (b) Schematic representation of the two surface models (Pb–X (X = I, Br)-rich and Cs–I-rich) in CsPbI$_3$ and CsPbBrI$_2$. (c) The bulk and surface binding energy of CsPbI$_3$ and CsPbBrI$_2$. (d) The displacement threshold energy of CsPbI$_3$ and CsPbBrI$_2$.

Perdew–Burke–Ernzerhof (PBE) functional for exchange–correlation. A supercell of 3 × 2 × 2 was created. It contains 12 formula units that were used to calculate formation energies. Plane waves with energies reaching 520 eV were employed to describe the electronic wave functions for CsPbI$_3$ and CsPbBrI$_2$. The Brillouin zone was sampled with 7 × 7 × 7 and 3 × 3 × 3 Monkhorst–Pack grids of k-points for geometry optimization and defect calculations, respectively. All structures were fully relaxed until the force converged above 0.05 eV/Å. The spin coupling effect must be considered to adequately represent the interaction between the magnetic moment of the electron spins and the atomic orbitals between Pb and X (X = Cl, Br, I), which is utilized to correct the final Hamiltonian energy and, more accurately, calculate the dielectric constant.[33] The AIMD was operated at the initial and final state temperatures of 300 and 600 K under the *NVT* ensemble, respectively, and the whole system relaxed for 6 ps. The displacement threshold energy was obtained by using the AIMD method based on the aBEST-master code.[34] The running times of *NVT* and *NVE* reached at least 6 ps.

MC Calculation Details. The results obtained from DFT were then transferred as the input parameters in the SRIM code. Figure S1 schematically illustrates the complete execution process in detail for carrying out the full destruction simulations. Irradiation calculations for damage detail events were executed by the SRIM code with H$^+$, and all flux was set as 10^5 p/cm^2. The material structure is shown in Figure S2, including the Au layer as the ohmic contact in the device and perovskite as the unit for photoelectric conversion. The simulation parameters included an irradiated area of 1 cm^2, and the device side length was 1 cm. Equation S11 quantifies the relationship between particle flux and irradiation damage. The densities of materials were ρ_{Au} = 19.31, $\rho_{\mathrm{CsPbI_3}}$ = 5.38, and $\rho_{\mathrm{CsPbBrI_2}}$ = 5.17,[35] and the thicknesses of the Au and perovskite layers were 800 Å and 3000 Å, respectively. The energies of the incident particles in the irradiation were 10 keV, 50 keV, 100 keV, and 1 MeV with directions as shown in Figure S3.

■ RESULTS AND DISCUSSION

The electric structure of α-CsPbI$_3$ (space group $Pm\bar{3}m$) was constructed according to the experimental data.[36] The CsPbBrI$_2$ structure was built by replacing the I atom with the Br atom and underwent sufficient structural relaxation to obtain α-CsPbBrI$_2$; the crystal structures are shown in Figures 1a and 1b. The basic information on these two perovskites was calculated in the ground state. The optimized lattice constants of CsPbI$_3$ were $a = b = c$ = 6.29 Å and of CsPbBrI$_2$ were a = 5.96 Å and $b = c$ = 6.40 Å with spin–orbital coupling (SOC), which were consistent with previously reported values.[36,37] The electron localization function (ELF) method was employed to analyze interatomic bonding.[38,39] The discrepancy of Pb–I (X = I, Br) interactions between CsPbI$_3$ and CsPbBrI$_2$ was further analyzed and is shown in Figures 1c and 1d. The ELF of the (100) lattice plane found that both systems showed typical ionic bonding between Pb–I. The minimum value of the ELF free electron region between Pb–I atoms was 0.29 in CsPbBrI$_2$ compared with 0.35 in the CsPbI$_3$ system, indicating strong electron localization around the Br-containing compound. To clarify the critical role of Br in the regulation of the valence band (VB) and conduction band (CB), DFT was used to calculate the density of states (DOS) of CsPbI$_3$ and CsPbBrI$_2$ in Figures 1e and 1f. The I 5p orbital mainly contributed to the

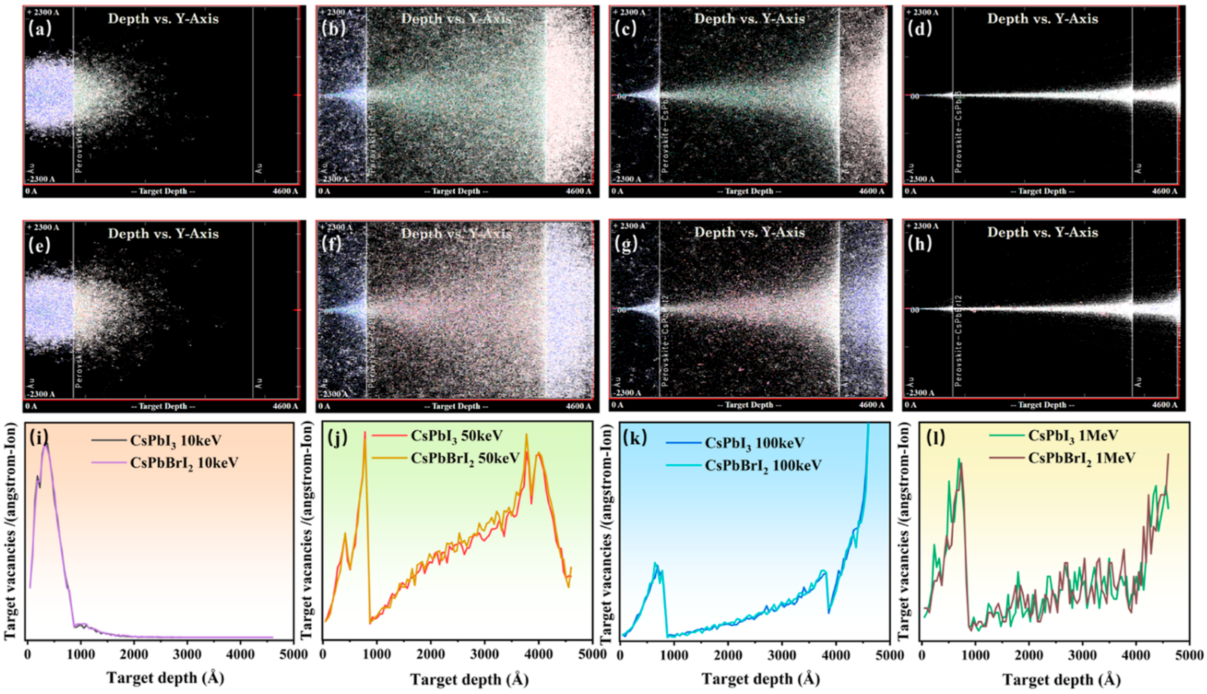

Figure 3. Damage depth under irradiation with (a)10 keV, (b) 50 keV, (c) 100 keV, and (d) 1 MeV of $CsPbI_3$; (e)10 keV, (f) 50 keV, (g) 100 keV, and (h) 1 MeV energy incident particles; the number of vacancies of $CsPbI_3$ and $CsPbBrI_2$ at (i)10 keV, (j) 50 keV, (k) 100 keV, and (l) 1 MeV.

valence-band maximum (VBM), whereas the main contribution of the conduction-band minimum (CBM) was the Pb 6p orbital. Figure 1f shows that the contribution of Br to VBM was lower than the I atom. The partial density of states (PDOS) results showed that the VBM was composed of Pb 6s−I 5p antibonding states, which was consistent with the results of previous research.[37] The electron transfer was further quantitatively analyzed, and the results are shown in Figure 1g. Following the addition of Br to the lattice, an increase in the number of lost electrons was observed in the Cs and Pb atoms. The transfer process occurred between Pb−I and Pb−Br, with a significantly higher electron transition for Br. This phenomenon can be attributed to the higher electronegativity of the atoms, which facilitates more significant electron gain during ionic bonding interactions. Ionic force enhancement inhibits irradiation-induced dissociation, explaining why $CsPbBrI_2$ is more stable than $CsPbI_3$ at room temperature.[40] The results suggested that electronegativity calculation on the atomic scale derived from Bader analysis can serve as an effective criterion for screening AIP components to optimize phase stability.

The accuracy of the full destruction simulation depends on the DFT-derived parameters characterizing atomic bonding disruption. Accordingly, both bulk and surface binding energies along with displacement threshold energy values were further calculated by DFT. A notable discrepancy exists in the binding energy of atoms within the material's bulk and surface regions. The binding energy of bulk atoms was calculated by utilizing the periodic lattice like Figure 2a, which exhibits the atomic structure model of $CsPbI_3$ and $CsPbBrI_2$ containing one I vacancy. However, the calculation of the binding energy on the surface requires a distinction between different atomic environments. Previous studies have shown that the Pb−*X* (*X* = I, Br) octahedral structure is more energetically stable, especially (001), which is the most stable lattice plane.[37,41] Two types of surfaces were constructed as Cs−I-rich and Pb−*X*-rich for calculation based on (001), as shown in Figure 2b. The formula of calculations can be expressed as eq S1 with perfect lattice and surface models. The atomic binding energy in the surface used the average values of Cs−I-rich and Pb−*X*-rich surfaces for meeting the MC simulation.

Figure 2c summarizes the results, showing that the I atom is more likely to break the bond in both bulk and surface systems. The binding energy values of the bulk system are higher than the surface, indicating that the bonding break of the internal position is more challenging than that in the surface. Notably, the energy (2.62 eV) of the I atom in the $CsPbBrI_2$ system exceeds that in $CsPbI_3$ (1.85 eV) in the bulk system, and the Br atom in the $CsPbBrI_2$ was among the second lowest compared with the Cs, I, and Pb, which is consistent with our Bader analysis confirming Br enhances the ionic interaction in the octahedron. However, the binding energy of I (1.19 eV) is slightly higher than that of Br (1.18 eV) on the surface, and Cs and Pb atoms were significantly higher than I and Br in both $CsPbI_3$ and $CsPbBrI_2$. While the binding energy of $CsPbBrI_2$ at the surface remains slightly higher than that of $CsPbI_3$, this discrepancy value is reduced. The results establish a clear dissociation hierarchy: irradiation-induced damage preferentially initiates at the Pb−I pair, followed by the Pb−Br pair. $CsPbI_3$ and $CsPbBrI_2$ exhibit slightly higher binding energy at surface sites of Pb−*X* than Cs−*X*. The results suggest that the Pb−*X* octahedron of $CsPbBrI_2$ requires greater dissociation energy, with Pb−*X* demonstrating enhanced stability over the Cs−*X*-rich surface, which agrees with the previous reports.[41,42] Furthermore, the minimum initial velocity of atomic displacement is employed by the *NVT* combined with *NVE* to calculate the displacement threshold energy. As demonstrated in Figure 2d, halogen atoms show the lowest displacement threshold energies with I being more susceptible to displacement than Br. The displacement threshold energy of Pb in $CsPbI_3$ (21.9 eV) is significantly higher than that of $CsPbBrI_2$

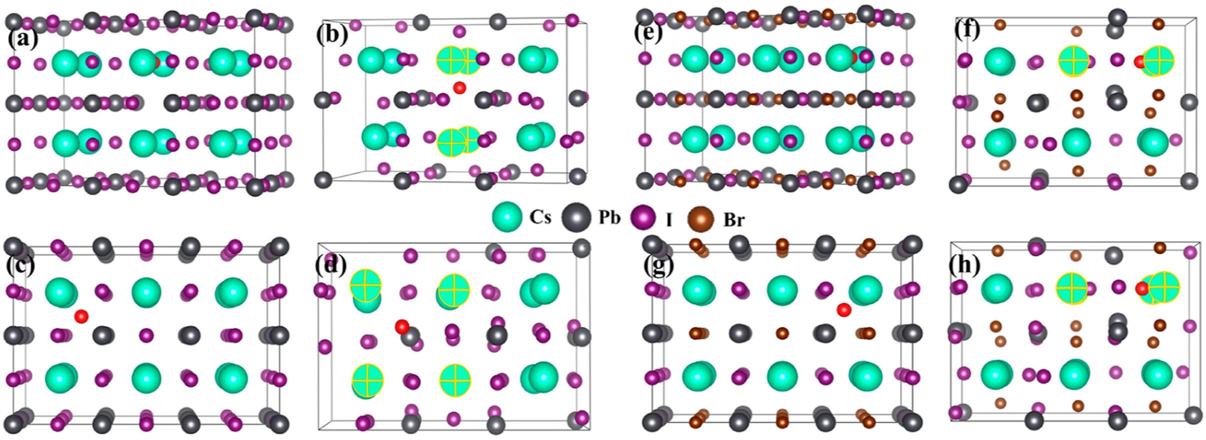

Figure 4. Structure of Frenkel defects is presented in $CsPbI_3$ and $CsPbBrI_2$; (a) and (c) are the Frenkel structures including the interstitial atom at the 8*g* and 3*c* Wyckoff positions in $CsPbI_3$; (b) and (d) are the relaxation structure of (a) and (c) in $CsPbI_3$; (e) and (g) are the Frenkel structures including the interstitial atom at the 8*g* and 3*c* Wyckoff positions in $CsPbBrI_2$; (f) and (h) are the relaxation structure of (e) and (g) in $CsPbBrI_2$. The red atom represents the interstitial atom of Frenkel defects, which layer was located by the marked Cs atoms.

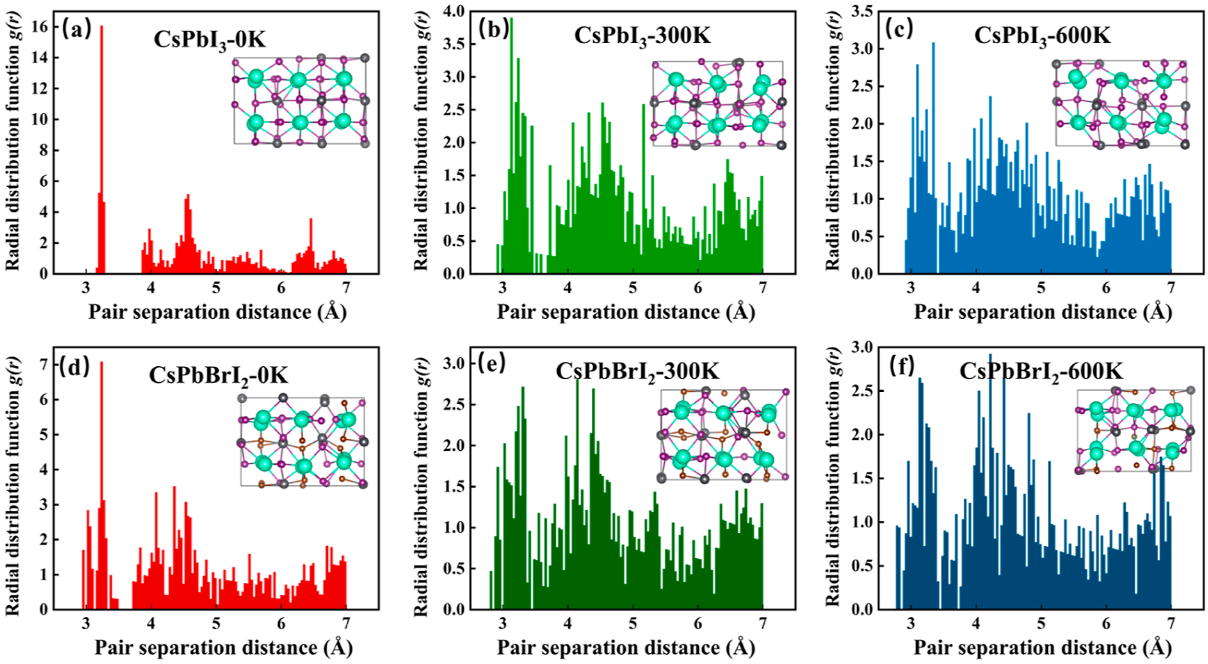

Figure 5. Lattice distortion caused by Frenkel defects after 6 ps of complete relaxation of AIMD: $CsPbI_3$ system at (a) 0 K, (b) 300 K, and (c) 600 K and $CsPbBrI_2$ system at (d) 0 K, (e) 300 K, and (f) 600 K.

(19.55 eV). These findings contradict the conclusions drawn from binding energy trends, which suggest that the dominant mechanisms underlying dissociation and displacement are entirely different. While it is evident that the energy expended in bond breaking during atomic displacement constitutes a significant component of the overall process, it is crucial to acknowledge the potential of resistance to atomic movement. This resistance might be attributed to the larger ionic radius of the I atom, which induces greater lattice strain during displacement in the $CsPbI_3$ system. Similarly, the Cs atoms exhibit high displacement thresholds due to the interaction with the octahedron by van der Waals coupling of its Wyckoff position (1*b* in space group $Pm\bar{3}m$) and atomic radius, which places the displacement in terms of high energy landscape dynamics.

MC was employed to describe the difference in displacement damage between $CsPbI_3$ and $CsPbBrI_2$. SRIM code was set for particle incident energies of 10 keV, 50 keV, 100 keV, and 1 MeV, respectively. The final damage results are shown in Figure 3. The maximum irradiation damage occurred at 50 keV, which means the entire energy is deposited inside the device (Figure 3b,f). Upon reaching an energy of 1 MeV, the incident particle directly penetrates the device, as shown in Figures 3d and 3h. The most significant damage happened between 50 and 100 keV. Statistical analysis revealed comparable displacement counts between the Pb−*X* pair, indicating similar radiation resistance under 10 keV (Figure 3i), even when the incident energy reaches 100 keV and 1 MeV. The discrepancy between $CsPbI_3$ and $CsPbBrI_2$ in terms of displacement damage is not particularly pronounced. A disparity of displacement damage was shown at 50 keV (Figure

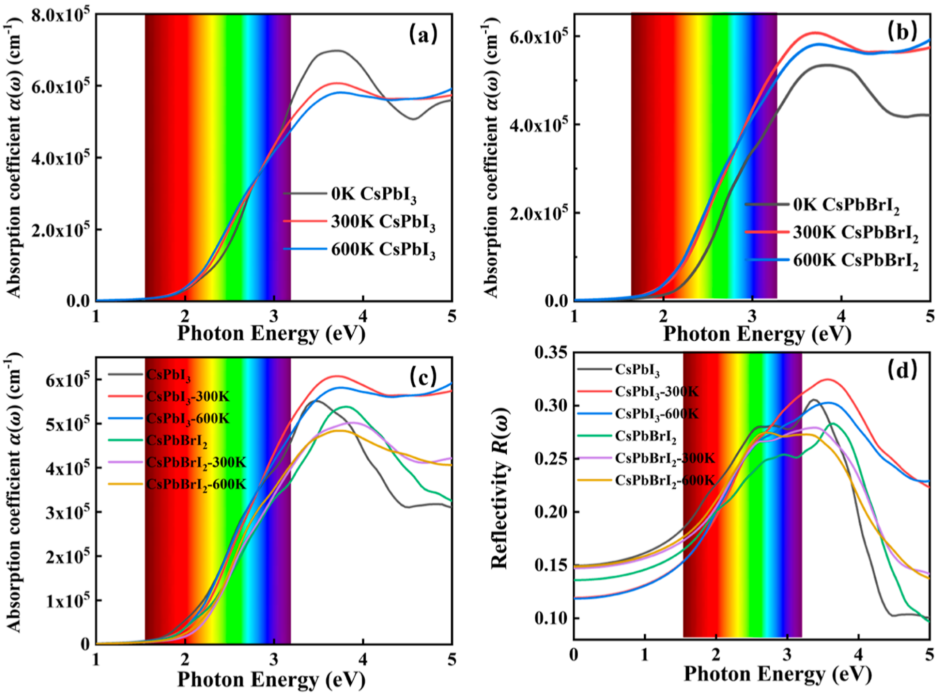

Figure 6. Calculated absorption coefficient of (a) $CsPbI_3$ and (b) $CsPbBrI_2$ with different temperatures, (c) absorption coefficient of thermal relaxation systems and perfect crystal systems, and (d) reflectivity of different temperature systems and perfect crystal systems.

3j) in depth between 2700 and 3800 Å, with $CsPbBrI_2$ exhibiting a higher displacement of atoms than $CsPbI_3$. The evidence indicates that displacement damage is the predominant form in perovskites within the energy range of 50 keV to 1 MeV, thereby confirming that the initial damage is located at the displacement of the halogen atoms. Similar results have reported that displacement damage to I atoms dominated $MAPbI_3$, whereas the damage for Pb was not significant under low-energy electron irradiation.[23,43] In summary, our findings indicated that $CsPbBrI_2$ had relatively significant displacement damage compared to $CsPbI_3$ under high-energy irradiation. Although $CsPbBrI_2$ exhibits more robust ionic bonding properties during electron transfer, once the interatomic irradiation dissociation process is completed, the atoms of $CsPbBrI_2$ might produce more atomic displacement relative to $CsPbI_3$ under sustained specific energy irradiation.

To elucidate the atomic-scale mechanisms of displacement damage in $CsPbI_3$ and $CsPbBrI_2$, a Frenkel defect of the I atom was inserted into the matrix for simulating the one event of displacement damage. Two types of neighboring interstitial positions (3*c* (between Cs−Cs) and 8*g* (Cs−Pb) of the Wyckoff position) were initially calculated, as was shown in Figure S4. The interstitial energies of the I atom at 3*c* and 8*g* in the crystalline structure of $CsPbI_3$ were 0.76 and 0.48 eV, while the energies were 0.38 and 0.03 eV for $CsPbBrI_2$, respectively, which means the defect tolerance of $CsPbBrI_2$ has an energetic advantage for interstitial atom relaxation. The generation of vacancies is initiated with I atoms of the nearest neighboring lattice, with the subsequent filling of the interstitial position occurring at positions 3*c* and 8*g*, like in Figure 4a,c,e,g. It is noteworthy that the interstitial position following relaxation atoms exhibits a degree of similarity, situated close to 24*l* (Figure S5) in the Wyckoff position, which can be seen in Figure 4b,d,f,h. The Frenkel defect formation energies of $CsPbI_3$ were 0.853 and 1.195 eV in the 8*g* and 3*c* positions, respectively, which is close to the reported value.[44] The Frenkel defects formation energies of $CsPbBrI_2$ were found to be 1.28 and 1.301 eV in the 8*g* and 3*c* positions, respectively, which was higher than the formation energies observed in $CsPbI_3$. The results can be inferred that the 24*l* position has the potential to accommodate I atoms, which are more readily implicated in the formation of Frenkel defects.

The lattice distortion of $CsPbI_3$ and $CsPbBrI_2$ was studied to understand the structural damage of Frenkel defects by the AIMD under 0 K, 300 K, and 600 K, as shown in Figure 5. The value of 0 K represents the absence of any thermodynamic factors during structural evolution. The distribution pattern of the atoms in the Pb-−*X* nearest neighbors (NN) was characterized by the radial distribution function (RDF). From Figures 5a and 5d, the lattice distortion of $CsPbBrI_2$ was found to be more significant than $CsPbI_3$, which was exacerbated at 300 K (Figure 5b,e) than at 0 K for both $CsPbI_3$ and $CsPbBrI_2$. Subsequently, the lattice distortion becomes larger in $CsPbI_3$ and $CsPbBrI_2$ with thermal relaxation at 600 K, as shown in Figures 5c and 5f. The relaxation structure after thermal analysis is shown in the inset image. The RDF results showed that the main atomic pair generating the displacement is 1NN (2.8−3.2 Å). The integration of the RDF concludes that an enlarged integration area and a heightened half-width imply a greater incidence of lattice distortions. The statistical results are presented in Table S1, demonstrating a significant increase in lattice distortion after thermal relaxation at temperatures of 300 K and 600 K in 6 ps. The bond length in Figure S6 shows that the maximum displacement distances of Pb−I and Pb−Br pairs are beyond 20%, consistent with the typical characteristics of irradiation amorphization in irradiation damage.[45,46] However, the lattice distortion produced at 300 K and 600 K compared to that at 0 K, the rate of change of $CsPbBrI_2$ is less than that of $CsPbI_3$. The reason can be attributed to the substitution of Br along the *a*-axis direction, which caused the mismatch in the lattice constant. The squared mean square displacement (MSD) at 600 K of $CsPbI_3$

and $CsPbBrI_2$ was further obtained from AIMD (Figure S7). The results showed that the displacement of I and Br atoms generated by the $CsPbBrI_2$ system was more than that of I atoms in $CsPbI_3$, which meant that more atoms in $CsPbBrI_2$ exceeded the vibration modulus to diffusion. And the bonding length change between Pb−I and Pb−Br is beyond 20%, which exhibited an amorphization characterization.[45,46] Moreover, the results showed that the average ionic mobility of I and Br in $CsPbBrI_2$ was 0.142×10^{-3} $cm^2/s/V$, which was higher than 0.114×10^{-3} $cm^2/s/V$ of I in $CsPbI_3$. The average diffusion coefficient was 0.734×10^{-5} cm^2/s in $CsPbBrI_2$, which was higher than 0.590×10^{-5} cm^2/s in $CsPbI_3$. According to the Arrhenius equation, $D = D_0 \exp\left(\frac{-E_a}{\kappa T}\right)$. The results reflected a more favorable energy landscape E_a in terms of the thermodynamic diffusion of Br, which caused more significant lattice distortion with ion migration. This might be attributed to Br ions having a smaller ionic radius relative to I. In other words, the formation of structure created by I displacement facilitated the migration of Br. Therefore, the increased lattice distortion by the movement of Br in the lattice positively affects its stability and optical properties. Overall, the lattice distortion in both $CsPbI_3$ and $CsPbBrI_2$ systems increased as the temperature increased, which meant that Frenkel defects suffered thermal influence and caused significant irradiation amorphization.

The lattice distortion will further influence the dielectric function (DF) form. Therefore, the absorption coefficients and reflectivity of $CsPbI_3$ and $CsPbBrI_2$ were calculated based on the structure obtained from AIMD. Figure 6a shows the absorption coefficients for $CsPbI_3$ in the visible light region (1.55−3.1 eV). The absorption coefficients at 300 and 600 K are higher than 0 K, indicating that their optical absorption properties were better after thermal relaxation (1.55−2.82 eV). The transition point of light absorption existed at 2.82 eV, at which the absorption coefficient decreased rapidly post thermal relaxation at 600 K. Unrelaxation systems of $CsPbI_3$ had a higher absorption peak in the ultraviolet (UV) region, indicating a higher absorption in UV than the thermal relaxation systems. The previous report suggests that UV solid absorption might hurt the stability of perovskites.[6] Furthermore, a similar phenomenon occurred in $CsPbBrI_2$, which has higher values of absorption coefficients at 300 and 600 K than at 0 K in the visible light region (1.55−3.1 eV), as shown in Figure 6b. The absorption coefficient at 600 K is very close compared to 300 K with a slight decrease after 2.86 eV in $CsPbBrI_2$. Therefore, we inferred that thermal treatment similar to an annealing process effectively restored the optical absorption properties in the visible light region after the formation of Frenkel defects.

Based on the above-mentioned results, a comparison of the thermal relaxation systems with a perfect crystal of $CsPbI_3$ and $CsPbBrI_2$ is shown in Figure 6c. $CsPbI_3$ with perfect crystalline structure had better optical properties than perfect crystalline $CsPbBrI_2$, which agrees with previous studies.[37] $CsPbI_3$ exhibited slightly higher absorption coefficients at 600 K thermal relaxation compared with those at 300 K thermal relaxation in the visible light region. At the same time, $CsPbI_3$ postthermal relaxation was higher than that of the perfect crystal after the photon energy reached 2.82 eV. Although the thermal treatment had a favorable effect on the maintenance of light absorption, the UV absorption of the irradiated system increased compared with that of a perfect crystal. The thermal relaxation of $CsPbBrI_2$ under 600 K reduced the absorption in the UV region but maintained its visible light absorption. Therefore, thermal relaxation after forming Frenkel defects in $CsPbBrI_2$ is a very effective method to maintain the optical properties after radiation exposure. The Pb−I and Pb−Br octahedra in Figure 5 show the degree of lattice distortion. However, the optical properties are not significantly impacted by this distortion. Consequently, the defect in question does not cause nonradiative loss. On the other hand, the Pb−Br system exhibits a somewhat increased light absorption coefficient, indicating that the energy level of the Br-induced defects offsets the negative impact of octahedral distortion. One possible explanation is that the synergetic effect of "irradiation-annealing" is the partial compensation by the displacement atoms produced in the inorganic Pb−I octahedral framework.[24,47−49] The phenomenon is more significant in $CsPbBrI_2$, which might benefit from the migration of Br under a thermal influence. Figure 6d shows the reflectivity variation of thermal relaxation and perfect crystal. The thermal treatment of $CsPbI_3$ can reduce the reflectivity value, especially for a 600 K thermal relaxation. Even the reflectivity increased in reverse, which is why the volume of $CsPbBrI_2$ was smaller than $CsPbI_3$, making it challenging to reduce its reflectivity. In a word, this study found that the materials produced a significant lattice distortion at 600 K but did not cause a substantial degradation of light absorption.

■ CONCLUSION

Our research exhibited an assessment method to describe perovskite irradiation damage by combining DFT and MC. From the DOS, ELF, and Bader analyses, $CsPbBrI_2$ exhibits more robust ionic bonding properties due to its stronger electronegativity, contributing to enhanced stability and resistance to irradiation dissociation. However, once the displacement threshold is surpassed, the dynamic self-healing behavior enables more efficient defect compensation through thermally activated migration to maintain the optical properties, which becomes the dominant mechanism during the displacement damage stage. The results indicate that both $CsPbI_3$ and $CsPbBrI_2$ have a specific optical recovery ability when subjected to dissociation damage and even displacement damage; especially $CsPbBrI_2$ exhibits better recovery by moving with a more favorable landscape. Overall, the stronger ionic bonding of the octahedron in perovskites increases the energy barrier for bonding dissociation. A potential positive effect of "irradiation annealing" indicated that the system of $CsPb{-}Br_{3-x}{-}I_x$ has great stable optical performance as a radiation device. Our study provides a reference for the irradiation damage evaluation method for perovskite and complex element systems, potentially expanding the commercial viability of perovskite technologies in aerospace.

■ ASSOCIATED CONTENT

Supporting Information

The Supporting Information is available free of charge at https://pubs.acs.org/doi/10.1021/acs.jpca.5c01588.

Computational method and details, simulation execution flowchart, device structures, defect structures, and RDF results (PDF)

AUTHOR INFORMATION

Corresponding Authors

Feida Chen − *Department of Nuclear Science & Technology, Nanjing University of Aeronautics and Astronautics, Nanjing 211106, China; Key Laboratory of Advanced Nuclear Technology and Radiation Protection, Ministry of Industry and Information Technology, Nanjing 211106, China;* orcid.org/0000-0002-1926-8563; Email: fdchen@nuaa.edu.cn

Xiaobin Tang − *Department of Nuclear Science & Technology, Nanjing University of Aeronautics and Astronautics, Nanjing 211106, China; Key Laboratory of Advanced Nuclear Technology and Radiation Protection, Ministry of Industry and Information Technology, Nanjing 211106, China;* orcid.org/0000-0003-3308-0468; Email: tangxiaobin@nuaa.edu.cn

Authors

Yibo Wang − *Department of Nuclear Science & Technology, Nanjing University of Aeronautics and Astronautics, Nanjing 211106, China; Key Laboratory of Advanced Nuclear Technology and Radiation Protection, Ministry of Industry and Information Technology, Nanjing 211106, China*

Kun Yang − *Department of Nuclear Science & Technology, Nanjing University of Aeronautics and Astronautics, Nanjing 211106, China; Key Laboratory of Advanced Nuclear Technology and Radiation Protection, Ministry of Industry and Information Technology, Nanjing 211106, China;* orcid.org/0000-0003-0040-3523

Daniu Han − *Department of Nuclear Science & Technology, Nanjing University of Aeronautics and Astronautics, Nanjing 211106, China; Key Laboratory of Advanced Nuclear Technology and Radiation Protection, Ministry of Industry and Information Technology, Nanjing 211106, China*

Complete contact information is available at:
https://pubs.acs.org/10.1021/acs.jpca.5c01588

Author Contributions

Yibo Wang: Conceptualization, Software, Methodology, Validation, Formal analysis, Investigation, Data curation, Writing—original draft, Writing—review and editing, Funding acquisition. **Feida Chen:** Conceptualization, Writing—review and editing. **Kun Yang:** Writing—original draft, Writing—review and editing. **Daniu Han:** Investigation. **Xiaobin Tang:** Writing—original draft, Supervision, Project administration, Funding acquisition.

Notes

The authors declare no competing financial interest.

ACKNOWLEDGMENTS

This work was supported by the Fundamental Research Funds for the Central Universities (Grant No. 1006-YAH22061) and the Postgraduate Research & Practice Innovation Program of Jiangsu Province (Grant No. KYCX23_0368).

REFERENCES

(1) Tai, Q.; Tang, K. C.; Yan, F. Recent Progress of Inorganic Perovskite Solar Cells. *Energy Environ. Sci.* **2019**, *12* (8), 2375−2405.

(2) Ma, T.; Wang, S.; Zhang, Y.; Zhang, K.; Yi, L. The Development of All-Inorganic $CsPbX_3$ Perovskite Solar Cells. *J. Mater. Sci.* **2020**, *55* (2), 464−479.

(3) Perumal Veeramalai, C.; Feng, S.; Zhang, X.; Pammi, S. V. N.; Pecunia, V.; Li, C. Lead−Halide Perovskites for next-Generation Self-Powered Photodetectors: A Comprehensive Review. *Photonics Res.* **2021**, *9* (6), 968.

(4) Chen, J.; Zhang, W.; Pullerits, T. Two-Photon Absorption in Halide Perovskites and Their Applications. *Mater. Horiz.* **2022**, *9* (9), 2255−2287.

(5) Chen, J.; Liu, D.; Al-Marri, M. J.; Nuuttila, L.; Lehtivuori, H.; Zheng, K. Photo-Stability of $CsPbBr_3$ Perovskite Quantum Dots for Optoelectronic Application. *Sci. China Mater.* **2016**, *59* (9), 719−727.

(6) Tu, Y.; Wu, J.; Xu, G.; Yang, X.; Cai, R.; Gong, Q.; Zhu, R.; Huang, W. Perovskite Solar Cells for Space Applications: Progress and Challenges. *Adv. Mater.* **2021**, *33* (21), 2006545.

(7) Chen, R.; Hui, Y.; Wu, B.; Wang, Y.; Huang, X.; Xu, Z.; Ruan, P.; Zhang, W.; Cheng, F.; Zhang, W.; et al. Moisture-Tolerant and High-Quality a-$CsPbI_3$ films for Efficient and Stable Perovskite Solar Modules. *J. Mater. Chem. A* **2020**, *8*, 9597−9606.

(8) Wang, Y.; Chen, Y.; Zhang, T.; Wang, X.; Zhao, Y. Chemically Stable Black Phase $CsPbI_3$ Inorganic Perovskites for High-Efficiency Photovoltaics. *Adv. Mater.* **2020**, *32*, 2001025.

(9) Steele, J. A.; Jin, H.; Dovgaliuk, I.; Berger, R. F.; Braeckevelt, T.; Yuan, H.; Martin, C.; Solano, E.; Lejaeghere, K.; Rogge, S. M. J.; et al. Thermal Unequilibrium of Strained Black $CsPbI_3$ Thin Films. *Science* **2019**, *365* (6454), 679−684.

(10) Swarnkar, A.; Marshall, A. R.; Sanehira, E. M.; Chernomordik, B. D.; Moore, D. T.; Christians, J. A.; Chakrabarti, T.; Luther, J. M. Quantum Dot-Induced Phase Stabilization of α-$CsPbI_3$ Perovskite for High-Efficiency Photovoltaics. *Science* **2016**, *354*, 92−95.

(11) Li, Y.; Zhang, C.; Zhang, X.; Huang, D.; Shen, Q.; Cheng, Y.; Huang, W. Intrinsic Point Defects in Inorganic Perovskite $CsPbI_3$ from First-Principles Prediction. *Appl. Phys. Lett.* **2017**, *111* (16), 162106.

(12) Berhe, T. A.; Su, W. N.; Chen, C. H.; Pan, C. J.; Cheng, J. H.; Chen, H. M.; Tsai, M. C.; Chen, L. Y.; Dubale, A. A.; Hwang, B. J. Organometal Halide Perovskite Solar Cells: Degradation and Stability. *Energy Environ. Sci.* **2016**, *9* (2), 323−356.

(13) Yang, J.; Liu, X.; Zhang, Y.; Zheng, X.; He, X.; Wang, H.; Yue, F.; Braun, S.; Chen, J.; XuLiJin, J. Y. Y.; et al. Comprehensive Understanding of Heat-Induced Degradation of Triple-Cation Mixed Halide Perovskite for a Robust Solar Cell. *Nano Energy* **2018**, *54* (August), 218−226.

(14) Yang, J.; Bao, Q.; Shen, L.; Ding, L. Potential Applications for Perovskite Solar Cells in Space. *Nano Energy* **2020**, *76* (May), 105019.

(15) De Siena, M. C.; Klepov, V. V.; Stepanoff, S. P.; Bayikadi, K. S.; Pan, L.; Pandey, I. R.; Karki, S.; Chung, D. Y.; Wolfe, D. E.; Kanatzidis, M. G. Extreme γ -Ray Radiation Tolerance of Spectrometer-Grade $CsPbBr_3$ Perovskite Detectors. *Adv. Mater.* **2023**, *35* (38), 2303244.

(16) He, T.; Li, X.; Qi, Y.; Zhao, M.; Feng, M. Molecular Dynamics Simulation of Primary Irradiation Damage in Ti-6Al-4V Alloys. *Nucl. Eng. Technol.* **2024**, *56* (4), 1480−1489.

(17) Xing, T.; Liu, S.; Wang, X.; Adekoya, M. A.; Wang, C.; Li, H.; Meng, F.; Du, X.; Sun, Y.; Zhu, S.; et al. Molecular Dynamics Simulations of Displacement Damage in SiGe Alloys Induced by Single and Binary Primary Knock-on Atoms under Different Temperatures. *Radiat. Eff. Defects Solids* **2023**, *178*, 1384−1403.

(18) Agarwal, S.; Lin, Y.; Li, C.; Stoller, R. E.; Zinkle, S. J. On the Use of SRIM for Calculating Vacancy Production: Quick Calculation and Full-Cascade Options. *Nucl. Instrum. Methods Phys. Res., Sect. B* **2021**, *503* (July), 11−29.

(19) Chen, S. L. Low-Energy Atomic Displacement Model of SRIM Simulations. *Nucl. Sci. Technol.* **2021**, *32* (11), 119.

(20) Wang, Y.; Li, S.; Chen, F.; Yang, K.; Ge, G.; Tang, X.; Fan, M.; Huang, P. Unique Dislocation Loops Distribution of AlCrFeNiTix Eutectic High-Entropy Alloys under High-Temperature Ion Irradiation. *J. Alloys Compd.* **2023**, *958*, 170373.

(21) Zhang, Y. Y.; Chen, S.; Xu, P.; Xiang, H.; Gong, X. G.; Walsh, A.; Wei, S. H. Intrinsic Instability of the Hybrid Halide Perovskite Semiconductor $CH_3NH_3PbI_3$. *Chin. Phys. Lett.* **2018**, *35* (3), 036104.

(22) Xiao, C.; Li, Z.; Guthrey, H.; Moseley, J.; Yang, Y.; Wozny, S.; Moutinho, H.; To, B.; Berry, J. J.; Gorman, B.; et al. Mechanisms of Electron-Beam-Induced Damage in Perovskite Thin Films Revealed by Cathodoluminescence Spectroscopy. *J. Phys. Chem. C* **2015**, *119* (48), 26904−26911.

(23) Cai, Z.; Wu, Y.; Chen, S. Energy-Dependent Knock-on Damage of Organic-Inorganic Hybrid Perovskites under Electron Beam Irradiation: First-Principles Insights. *Appl. Phys. Lett.* **2021**, *119* (12), 123901.

(24) Brus, V. V.; Lang, F.; Bundesmann, J.; Seidel, S.; Denker, A.; Rech, B.; Landi, G.; Neitzert, H. C.; Rappich, J.; Nickel, N. H. Defect Dynamics in Proton Irradiated $CH_3NH_3PbI_3$ Perovskite Solar Cells. *Adv. Electron. Mater.* **2017**, *3* (2), 1600438.

(25) Dastidar, S.; Hawley, C. J.; Dillon, A. D.; Gutierrez-Perez, A. D.; Spanier, J. E.; Fafarman, A. T. Quantitative Phase-Change Thermodynamics and Metastability of Perovskite-Phase Cesium Lead Iodide. *J. Phys. Chem. Lett.* **2017**, *8* (6), 1278−1282.

(26) Yang, W.; Zhu, B.; Hou, Y.; Yang, X.; Pang, J. Ag Diffusion Effect on the Crystal Structure, Band Structure, and Optical Property of α-$CsPbI_3$ Perovskite Materials. *Phys. B Condens. Matter* **2020**, *579* (August 2019), 411917.

(27) Li, J.; Du, X.; Niu, G.; Xie, H.; Chen, Y.; Yuan, Y.; Gao, Y.; Xiao, H.; Tang, J.; Pan, A.; Yang, B. Rubidium Doping to Enhance Carrier Transport in $CsPbBr_3$ Single Crystals for High-Performance X-Ray Detection. *ACS Appl. Mater. Interfaces* **2020**, *12* (1), 989−996.

(28) Liu, D.; Zha, W.; Guo, Y.; Sa, R. Insight into the Improved Phase Stability of $CsPbI_3$ from First-Principles Calculations. *ACS Omega* **2020**, *5* (1), 893−896.

(29) Maughan, A. E.; Ganose, A. M.; Bordelon, M. M.; Miller, E. M.; Scanlon, D. O.; Neilson, J. R. Defect Tolerance to Intolerance in the Vacancy-Ordered Double Perovskite Semiconductors Cs_2SnI_6 and Cs_2TeI_6. *J. Am. Chem. Soc.* **2016**, *138* (27), 8453−8464.

(30) Fang, Z.; Shang, M.; Hou, X.; Zheng, Y.; Du, Z.; Yang, Z.; Chou, K. C.; Yang, W.; Wang, Z. L.; Yang, Y. Bandgap Alignment of α-$CsPbI_3$ Perovskites with Synergistically Enhanced Stability and Optical Performance via B-Site Minor Doping. *Nano Energy* **2019**, *61* (March), 389−396.

(31) Kresse, G.; Furthmüller, J. Efficiency of Ab-Initio Total Energy Calculations for Metals and Semiconductors Using a Plane-Wave Basis Set. *Comput. Mater. Sci.* **1996**, *6* (1), 15−50.

(32) Kresse, G.; Hafner, J. Ab Initio Molecular Dynamics for Liquid Metals. *Phys. Rev. B* **1993**, *47* (1), 558−561.

(33) Manchon, A.; Koo, H. C.; Nitta, J.; Frolov, S. M.; Duine, R. A. New Perspectives for Rashba Spin-Orbit Coupling. *Nat. Mater.* **2015**, *14* (9), 871−882.

(34) Pan, Y.; Lei, B.; Qiao, J.; Hu, Z.; Zhou, W.; Ji, W. Selective Linear Etching of Monolayer Black Phosphorus Using Electron Beams. *Chin. Phys. B* **2020**, *29* (8), 086801.

(35) Wang, X.; Li, H.; Xue, Z.; Xiang, Y.; Hu, X.; Li, Z.; Qin, H.; Qin, A.; Zhang, H. One-Dimensional Orthorhombic $CsPbI_3$ Polycrystalline Thick Film for Efficient and Highly Stable Direct X-Ray Detection and Imaging. *Chem. Eng. J.* **2024**, *486*, 150394.

(36) Trots, D. M.; Myagkota, S. V. High-Temperature Structural Evolution of Caesium and Rubidium Triiodoplumbates. *J. Phys. Chem. Solids* **2008**, *69* (10), 2520−2526.

(37) Chen, Y.; Shi, T.; Liu, P.; Xie, W.; Chen, K.; Xu, X.; Shui, L.; Shang, C.; Chen, Z.; Yip, H. L.; et al. The Distinctive Phase Stability and Defect Physics in $CsPbI_2Br$ Perovskite. *J. Mater. Chem. A* **2019**, *7* (35), 20201−20207.

(38) Savin, A.; Nesper, R.; Wengert, S.; Fässler, T. F. ELF: The Electron Localization Function. *Angew. Chem., Int. Ed. Engl.* **1997**, *36* (17), 1808−1832.

(39) Galbraith, J. M.; Schreiner, P. R.; Harris, N.; Wittkopp, A.; Shaik, S. A Valence Bond Study of the Bergman Cyclization: Geometric Features, Resonance Energy, and Nucleus-Independent Chemical Shift (NICS) Values. *Chem.—Eur. J.* **2000**, *6*, 1446−1454.

(40) Liu, X.; Li, J.; Cui, X.; Wang, X.; Yang, D. The Progress and Efficiency of $CsPbI_2Br$ Perovskite Solar Cells. *J. Mater. Chem. C* **2023**, *11* (2), 426−455.

(41) Yang, F.; Wang, C.; Pan, Y.; Zhou, X.; Kong, X.; Ji, W. Surface Stabilized Cubic Phase of $CsPbI_3$ and $CsPbBr_3$ at Room Temperature. *Chin. Phys. B* **2019**, *28* (5), 056402.

(42) Zhang, J.; Liu, X.; Jiang, P.; Chen, H.; Wang, Y.; Ma, J.; Zhang, R.; Yang, F.; Wang, M.; Zhang, J.; et al. Red-Emitting $CsPbBrI_2$/PbSe Heterojunction Nanocrystals with High Luminescent Efficiency and Stability for Bright Light-Emitting Diodes. *Nano Energy* **2019**, *66*, 104142.

(43) Milosavljević, A. R.; Huang, W.; Sadhu, S.; Ptasinska, S. Low-Energy Electron-Induced Transformations in Organolead Halide Perovskite. *Angew. Chem., Int. Ed.* **2016**, *55* (34), 10083−10087.

(44) Kaiser, W.; Hussain, K.; Singh, A.; Alothman, A. A.; Meggiolaro, D.; Gagliardi, A.; Mosconi, E.; De Angelis, F. Defect Formation and Healing at Grain Boundaries in Lead-Halide Perovskites. *J. Mater. Chem. A* **2022**, *10* (46), 24854−24865.

(45) Xiao, H.; Zhao, S.; Wang, Y.; Huang, Q.; Wang, C. The Critical Role of Irradiated Intermediate State Lattice Distortion on the Amorphization Resistance in MAX Phases. *Ceram. Int.* **2024**, *50* (22), 48779−48787.

(46) Jiang, C.; Zheng, M.-J.; Morgan, D.; Szlufarska, I. Amorphization Driven by Defect-Induced Mechanical Instability. *Phys. Rev. Lett.* **2013**, *111* (15), 155501.

(47) Yamaguchi, M.; Ando, K. Mechanism for Radiation Resistance of InP Solar Cells. *J. Appl. Phys.* **1988**, *63* (11), 5555−5562.

(48) Markvart, T. Radiation Damage in Solar Cells. *J. Mater. Sci. Mater. Electron.* **1990**, *1* (1), 1−12.

(49) Look, D. C.; Leedy, K. D.; Vines, L.; Svensson, B. G.; Zubiaga, A.; Tuomisto, F.; Doutt, D. R.; Brillson, L. J. Self-Compensation in Semiconductors: The Zn Vacancy in Ga-Doped ZnO. *Phys. Rev. B: Condens. Matter Mater. Phys.* **2011**, *84* (11), 115202.